Available online at www.sciencedirect.com
ScienceDirect
International Journal of Heat and Fluid Flow 29 (2008) 1103–1112
International Journal of HEAT AND FLUID FLOW
www.elsevier.com/locate/ijhff

Wavelet analysis of the surface temperature field at an air–water interface subject to moderate wind stress

Nicholas V. Scott *, Robert A. Handler, Geoffrey B. Smith

Naval Research Laboratory, Code 7233, 4555 Overlook Avenue, Washington, DC 20375, United States

Received 19 March 2007; received in revised form 19 November 2007; accepted 20 November 2007
Available online 15 February 2008

Abstract

A new analysis methodology based on the wavelet transform is used to estimate the cross-wind scale statistics of high surface temperature events from two-dimensional infrared imagery. The method is applied to laboratory data obtained from an experiment conducted in 2001 at the University of Miami, Rosenstiel School of Marine and Atmospheric Science Air–sea Interaction Saltwater Tank (ASIST). For the case of positive heat flux, in which heat is transported from water to air and for all wind forcing conditions, results from the analysis of infrared images show that the number of high temperature events, when scanned in the cross-wind direction, occupies a wide range of scales. For all wind cases, at a low temperature fluctuation threshold, the number of high temperature events increases with increasing wavenumber (decreasing scale). As the temperature fluctuation threshold is increased, this distribution collapses around a characteristic scale. In addition, as the wind speed increases this scale decreases. The statistical scale results are shown to be consistent with estimates of streak spacing based on a standard parameterization of the turbulent dynamics as well as with the results from numerical experiments. Our results suggest that further statistical analysis may possibly allow for the estimation of wind stress from infrared imagery.

Keywords: Wavelet transform; Coherent temperature groups; Temperature fluctuation threshold; Infrared imagery; Characteristic scale

1. Introduction

The transport of heat and gas across the air–water interface is a complex problem whose importance spans a variety of fields in science and engineering.

We are particularly concerned in this work with the frequently occurring situation in which heat is transported from the water column to the atmosphere. In this instance, a thin thermal boundary-layer, often called the 'cool-skin', develops at the water surface. This results in the surface temperature of the ocean being cooler than the bulk temperature of the water column. The opposite situation is that in which heat is transferred from the atmosphere to the water. In this case a 'warm-skin' is formed at the interface. The processes occurring within this thin thermal layer play a significant role in determining global mass and heat budgets from the very small scale to synoptic and decadal scales. More specifically, these processes are directly involved in determining the flux of heat and gases at the air–sea interface.

A major goal of research in this area has been to link air–sea fluxes to other more accessible parameters such as wind stress. One investigative route is via point measurements of the evolution of gas concentration in a saturated fluid layer. Since the Schmidt number of most gases in water is much larger than one, the mass transfer is primarily controlled from the water side of the interface. In this context, the classical measurement of the mass transfer coefficient has evolved from the measurement of the e-folding time scale associated with gas transport out of the water column. These measurements have revealed a variety of mechanisms which contribute to changes in mass

* Corresponding author. Present address: University of Florida, Civil and Coastal Engineering Department, Weil Hall, Gainseville, FL 32608. Tel.: +352 392 9537x1434.
E-mail address: nscott@whoi.edu (N.V. Scott).

0142-727X/$ - see front matter © 2008 Elsevier Inc. All rights reserved.
doi:10.1016/j.ijheatfluidflow.2007.11.002

transport. For example, Dickey et al. (1984) measured the gas transfer using this methodology along with the sub-surface turbulence statistics and found results that were consistent with the classical models of surface renewal and energy dissipation scaling. This technique pointed to the surface layer turbulent physics as being of great importance in controlling the gas and heat flux.

More innovative techniques of mass transfer measurement have progressed from these simple measurements towards identifying the enhancing effect of wind forcing and waves or surface geometry on the interfacial transport. For instance, Wanninkohf and McGillis (1999) used field measurements of gas transfer and found it to scale with the cube of the wind speed. They attributed this scaling to breaking surface gravity waves. Bock et al. (1999) went on to investigate the relationship between surface geometry noting the strong correlation between gas transfer and mean square slope of short wind waves produced in the laboratory. Melville et al. (1998) performed laboratory measurements of the generation and evolution of Langmuir circulation. Though their experiment was not explicitly designed to study the interfacial heat or mass transport, the occurrence of specific scales for Langmuir cells and surface streaks point to the importance of these structures to the dynamics of the momentum and thermal boundary-layer which control flux processes. All of these studies have revealed not only the richness of the processes at the air–sea interface and their relationship to mass transfer and indirectly heat transfer, but also the importance of understanding air–sea interfacial dynamics.

With the advent of new computer and optical technology, even greater progress has been made in the investigation of the surface layer temperature field and heat and mass transport. For example, McKenna and McGillis (2004) used digital particle image velocimetry to make measurements of surface divergence and produced evidence of a strong relationship between the ensemble averaged value of the magnitude of the surface divergence and the enhanced gas exchange coefficient. Infrared imagery, with its high spatial and temporal resolution along with the fact that it is a true 'surface' measurement, has been of vital importance. Jessup et al. (1997) used infrared technology to remotely quantify breaking wave dynamics by examining the surface disruption and recovery produced by breaking waves. Zappa et al. (2004) used the same type of infrared thermography to understand the role of microscale breaking waves in the enhancement of gas and heat transfer. Numerical simulations have played a role in extending our knowledge of the processes at the air–water interface and their connection to airside forcing. In particular, Handler et al. (2001) performed direct numerical simulations of low Reynolds number flow under a sheared interface with no surface waves. They found the presence of coherent temperature structures which had the shape of fish-scales throughout the two-dimensional spatial domain. These structures were consistent with the observations of Smith et al. (2007) who found the same type of fish-scale structures in laboratory experiments. This range of work has revealed the complex processes involving the flux of heat present near the interfacial region and the need for a fuller understanding of them.

There has been a great wealth of infrared imagery obtained to this point but very few mathematical methods of data analysis have been exploited in trying to investigate the interfacial heat transport. Komori et al. (1993) used the VITA technique in an attempt to establish a correlation between the mass transfer velocity and the frequency of surface renewal events. Some research has been carried out by Schimpf et al. (2004) who used Laplacian pyramids to recursively filter infrared thermographic images according to scale to understand the contribution of the various size scales to the surface layer temperature variance. In addition, Garbe et al. (2004) used passive thermographic techniques and digital image processing techniques to not only make measurements of oceanic and laboratory temperature fields but also to verify the surface renewal model of air–water heat exchange. These methods yielded new ways to infer interfacial heat flux. However, these studies have not provided an in depth analysis of the naturally occurring coherent temperature structures which appear (Handler et al., 2001).

Numerical simulations along with experimental investigations have shown a correlation between the change in scales of coherent thermal structures at the interface and wind shear (Handler et al., 2001; Tsai et al., 2005, and Smith et al., 2007). Such studies point to a need to develop not only a robust way to detect and quantify the temperature structures in the surface layer, but a way that, in principle, allows for the extrapolation of wind stress from their modulation in size. This is the main motivation for this paper. Direct observations of surface temperature have been made using a high resolution infrared sensor in a laboratory. We combine the results of this new technology with a new data analysis technique based on the wavelet transform (Scott et al., 2005) to examine the relationship of coherent surface layer temperature events to wind stress.

2. Experiment

The laboratory experiment conducted at the University of Miami, Rosenstiel School of Marine and Atmospheric Science was designed to investigate the dynamics of the surface layer temperature field under wind forcing. One of the aims of the experiment was the attainment of spatial temperature data in a laboratory for the improvement of parameterizations of gas and heat transfer. The infrared images were obtained from an Indigo Systems Merlin Mid-Wave IR sensor. The imager possesses a rectangular array size of 320×256 pixels which translates to a spatial resolution of 0.0907 cm/pixel in our experiment. The imager obtains snapshots of the water surface at a rate of 60 Hz and has a thermal sensitivity of about 0.02 °C. Further details concerning the camera and the experiment in general may be found in Smith et al., 2007.

Table 1
Table of experimental parameters for data cited

Cool skin	U (m s^{-1})	u_w^* (m s^{-1})	$\lambda^+ = \frac{100\nu}{u^*}$ (m)	T_{air}–T_w (°C)	Q (W/m^2)	$Ri = \frac{\beta g q_s \nu}{(u_w^*)^4 \rho_0 c}$
Case1	1.925	2.2×10^{-3}	4.55×10^{-4}	−14.24	393	7.0×10^{-3}
Case 2	3.977	4.3×10^{-3}	2.33×10^{-4}	−14.78	850	1.0×10^{-3}
Case 3	5.0031	5.7×10^{-3}	1.75×10^{-4}	−14.63	1144	4.0×10^{-4}
Case 4	7.0552	9.3×10^{-3}	1.08×10^{-4}	−14.69	1764	1.0×10^{-4}
Warm skin						
Case 5	2.951	3.1×10^{-3}	3.23×10^{-4}	9.731	−140	-6.0×10^{-4}

A table of conditions for the five different cases is shown in Table 1. Four data sets were from the unstable scenario of a cool-skin layer above a bulk layer of warm fluid where the temperature differences were on the order of 1.5 °C. One data set from the stable case of a warm-skin layer above a cooler fluid bulk layer was also used where the temperature differences were on the order of 0.25 °C. Each data set corresponds to a different wind speed and heat flux and therefore a different flux-based Richardson number defined by:

$$Ri = \frac{\beta g q_s \nu}{(u_w^*)^4 \rho_0 c}, \tag{1}$$

where the quantities β, g, q_s, u_w^*, ρ_0, c and ν are the coefficient of thermal expansion, gravitational acceleration, heat flux, friction velocity in water, water density, the specific heat of water, and water viscosity respectively. The quantity u_w^* is defined as $u_w^* = \sqrt{\frac{\tau}{\rho_0}}$ where τ is the shear stress at the air–water interface. From this point onwards the experimental runs for each Richardson number will be designated by case 1, case 2, etc. as defined in Table 1.

At low to moderate mean wind speeds the surface temperature field, as viewed by the infrared camera, possesses a coherent fish-scale temperature pattern described above. This is illustrated in Fig. 1a. In this figure the camera was oriented such that the wind moved from the upper left of the image towards the lower right. The resulting structures align themselves with the wind and exhibit a quasi-periodicity in the cross-wind direction. They appear to possess a width that is hypothesized to be inversely proportional to wind stress and directly proportional to viscosity via the parameterization given in Handler et al. (2001). Simple Fourier analysis of the cross-wind structure of the infrared temperature field failed to clearly define a spatial scale, so a local analysis based on the wavelet transform was conducted. The methodology used here is very similar to that used by Scott et al. (2005), where a wavelet transform was applied to spatial measurements of the oceanic surface wave field to detect steep surface wave crests and to quantify their scale. Here we apply a similar type of analysis to infrared surface temperature measurements taken from the five data sets.

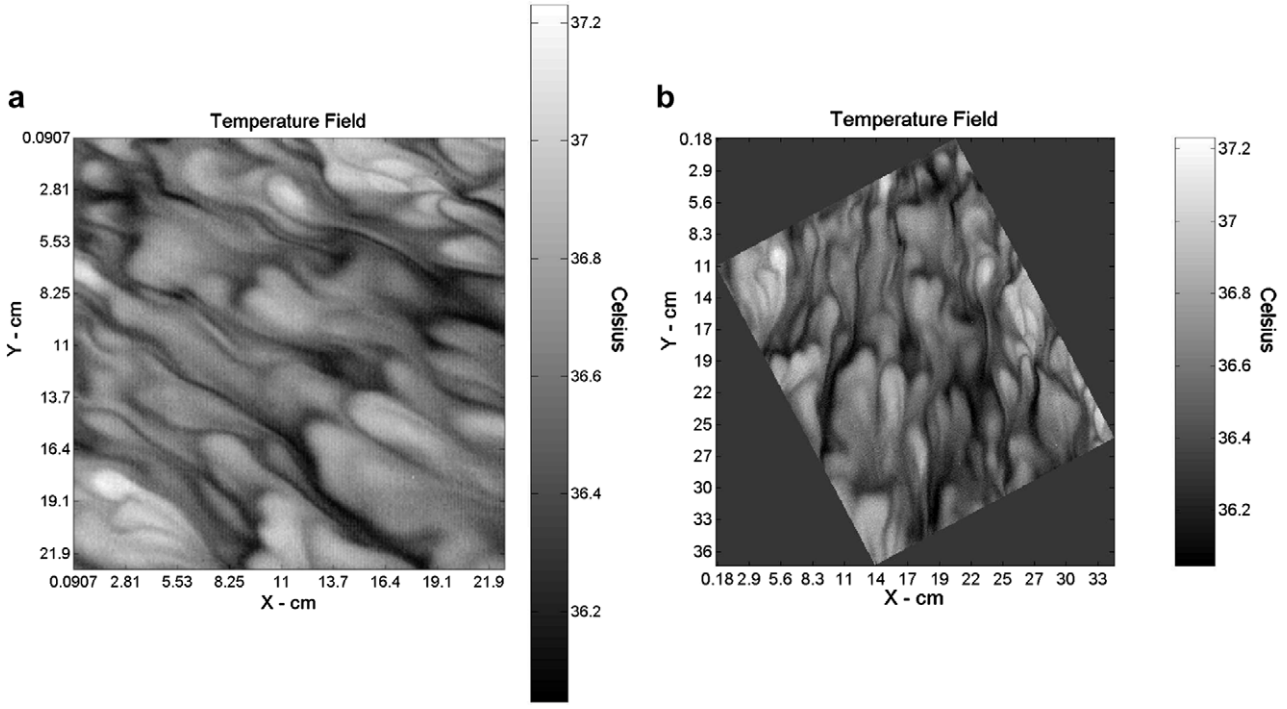

Fig. 1. (a) Infrared image of water surface with mean wind speed of 1.9 m s^{-1} and (b) rotated infrared image of the same water surface.

3. Data analysis

3.1. Wavelet transform

The original motivation for the use of the wavelet transform was the desire to obtain local cross-wind scale information from a temperature signal taken from infrared images. The wavelet transform of a spatial temperature signal $s(u)$ in this study is defined as

$$Ws(a,x) = \int_{-\infty}^{\infty} s(u)\frac{1}{a}\Psi\left(\frac{u-x}{a}\right)\mathrm{d}u. \tag{2}$$

Here $\Psi(a,x)$ is the Morlet mother wavelet defined in this study as

$$\Psi(a,x) = \Psi\left(\frac{x}{a}\right) = \mathrm{Real}\left[\mathrm{e}^{\mathrm{i}2\pi K_0\frac{x}{a}}\mathrm{e}^{-\frac{1}{2}\left(\frac{x}{a}\right)^2}\right], \quad K_0 = 1. \tag{3}$$

We note the original mathematical form of the Morlet wavelet as formulated by Goupillaud et al. (1984) has the form

$$\Psi(a,x) = \Psi\left(\frac{x}{a}\right) = Be^{-\frac{1}{2}\left(\frac{x}{a}\right)^2}\left[\mathrm{e}^{\mathrm{i}2\pi K_0\frac{x}{a}} - \kappa\right], \tag{4}$$

where $\kappa = \mathrm{e}^{-\frac{1}{2}(2\pi K_0)^2}$ and $B = \pi^{-\frac{1}{4}}\left(1 + \mathrm{e}^{-(2\pi K_0)^2} - 2\mathrm{e}^{-\frac{3}{4}(2\pi K_0)^2}\right)^{-\frac{1}{2}}$. Since $2\pi K_0 > 5$, $\kappa < 10^{-5}$ is negligible and therefore this term is neglected in Eq. (3). The wavenumber of the Morlet wavelet is K_0, the variable 'a' is a scaling parameter, and the spatial coordinate is designated by the variable x. The wavenumber associated with the fluctuations in the structure of the temperature signal is defined as

$$k = \frac{1}{\lambda}, \tag{5}$$

where

$$\lambda = \frac{a}{K_0}. \tag{6}$$

The wavenumber 'k' therefore has a one to one relationship with the scale parameter 'a'.

We note that the Morlet wavelet, as defined here, is the real part of a complex quantity and is used since we are concerned only with quantifying the cross-wind scale of the temperature fluctuations from the mean. The normalization used here is different from the classical $\frac{1}{\sqrt{a}}$ energy preserving normalization. The wavelet transform $Ws(a,x)$ preserves the amplitude of the fluctuation of the signal, $s(u)$, in the sense that signals of different scales but the same deviation from the mean possess the same wavelet transform (Scott, 2005).

The Morlet wavelet is a solution to the linear wave theory equations and is used because of its characteristic feature of resembling a compact periodic group of fluctuations. When applied to a signal it effectively searches the signal and finds regions where the data has wave-like characteristics. In addition, if the signal is interpreted as temperature, the local peak value of the inner product of the signal and the Morlet wavelet produces a measure of the average temperature fluctuation over the support of the wavelet. Thus, a signal with a high temperature event with scale a_0 and position x_0 will have a wavelet transform characterized by a large peak value of Ws at (a_0, x_0), and the peak value is proportional to the average temperature fluctuation of the signal in the neighborhood of x_0. In addition, two sinusoidal signals whose temperature amplitude fluctuations are equal will have equal peak values of $Ws(a,x)$ at each of the signals' respective scales. The preservation of the signal's average temperature deviation from the mean in the 'local' sense as described here allows for the detection of high temperature events associated with coherent temperature groups in the data.

3.2. Wavelet analysis of the temperature field

The continuous wavelet transform, as delineated in Eqs. (2) and (3), is implemented in a discretized version using the Matlab 5.3 wavelet toolbox software. The continuous wavelet transform allows for the continuous and redundant unfolding of information in both scale and space. This in turn enables the dynamical tracking of coherent structures. Wavelet analysis was performed on temperature signals which were extracted from a set of images. Before this was done, a simple autocorrelation of single temperature values in a sequence of images over time was performed to assess the point in time in which the images became statistically independent. Every 25th image was found to be statistically independent and on this basis 45 statistically independent images were selected to undergo wavelet analysis. These images were subsequently rotated such that the mean wind direction was directed vertically downward as shown in Fig. 1b.

If we define a coordinate system such that x is the horizontal coordinate and y is the vertical coordinate parallel to the wind direction, a temperature–space series $s(x)$ can be described by:

$$s(x) = K \times (S(x,y_0) - \overline{S}(y_0)), \tag{7}$$

where S is the raw thermal data, $\overline{S}$ is the mean value of the data taken at a fixed vertical coordinate y_0, and K is a conversion constant (0.02 °C/count). Thus the data analyzed, $s(x)$, is in units of degrees Celsius.

The Morlet wavelet transform was performed on each temperature–space series over a set of discrete scales (with a constant Δa in log space) that extends from 0.1362 cm^{-1} to a limiting wavenumber of 4.2 cm^{-1}. This wavenumber range was obtained from performing Fourier analysis and inspecting the power spectrum to find the biggest scales resolvable in the data set and the smallest scales before the noise floor occurs. The extracted temperature–space series were subject to edge effects at the boundaries, especially at large scales, due to the 'start up' process of the convolution. This edge effect takes the form of a cone of influence (Addison, 2002) which produces a linearly decreasing region of contamination as the scale is decreased. We calculated the cone of influence for the largest scale used in the analysis. This was done by taking the largest scale

of the wavelet transform and a sinusoid of corresponding scale and estimating the point at which the amplitude of the sinusoid decreased by e^{-2}. This is similar to the work of Grinsted et al. (2004). We chose to use only the statistics that started from the higher wavenumber of $0.2\,\mathrm{cm}^{-1}$ which corresponds to truncating 5 cm of data from each side of the temperature space series. This truncated region represents the maximum contaminated region of the wavelet transform since it is associated with the largest scale.

The conversion from the wavelet transform threshold to the real temperature fluctuation threshold is accomplished by first taking a pure sinusoid $s(u) = A\sin(ku)$ of known temperature amplitude A and wavenumber k, and obtaining the wavelet transform of the signal, $Ws(a,x)$. The peak value of the wavelet transform is then related to the temperature fluctuation amplitude in order to determine the conversion constant χ:

$$\chi = \frac{A}{\max[Ws(a,x)]} \tag{8}$$

With real temperature data, this constant is used to convert from the local maximum value of the wavelet transform to the equivalent temperature fluctuation threshold. This temperature fluctuation threshold represents the temperature amplitude, or temperature deviation from the mean, that a temperature sinusoidal signal of a scale equivalent to the real temperature–space series would possess. The proof of this, albeit applied to surface gravity wave fluctuations, can be found in Scott (2005).

A typical example of a wavelet transform is shown in Fig. 2 along with a plot of the temperature signal from case 1 from which it was computed. The wavelet transform contains an array of high temperature events designated by local maxima. In order to obtain a distribution of these events, a temperature fluctuation threshold is applied. Thus all points with a wavelet transform value above the set threshold are selected. These points appear as aggregates in local regions of $Ws(a,x)$ enclosed by the dashed lines shown in Fig. 2. From these groups of points, the highest value is sought. The highest values or local maxima throughout the wavelet transform are obtained by using a nine-point box filter. The filter is moved throughout the transform and from these groups, only those points that are larger than the surrounding eight points are selected. The local maxima selected in the manner described above appear as asterisks in Fig. 2. Since the Morlet wavelet in this study is a compact group of temperature fluctuations, these asterisks are defined as individual high temperature events associated with cohesive temperature groups in the subsequent analyses.

Each high temperature event in a temperature signal, denoted by asterisks in Fig. 2, has associated with it a scale value and spatial position. Thus after wavelet transformation, each temperature–space series denoted by an index 'j' can be converted to $H_T^j(k)$ $j = 1,2,3,\ldots$., the number of events of wavenumber k exceeding a set high temperature fluctuation threshold T. The final statistic H_T (k) is obtained by averaging the individual distributions over 100 temperature–space series per image and over 45 statis-

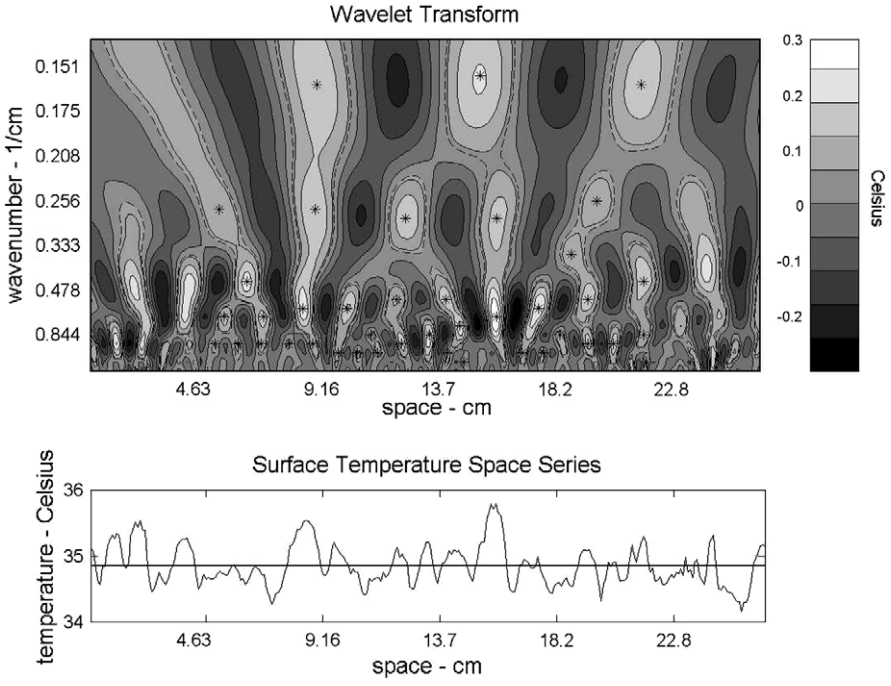

Fig. 2. Wavelet transform of temperature signal from infrared image of water surface with mean wind speed of $2.9\,\mathrm{m\,s}^{-1}$. Asterisks delineate high temperature events with events in the contaminated regions not shown. Temperature threshold of 0.05 °C is designated by dotted line. Contours drawn at every 0.074 interval.

tically independent images. Finally, we divide by the area of an individual image thus obtaining $H_T(k)$ in units of events per square centimeter.

4. Results and discussion

4.1. Detection of high temperature events

The wavelet analysis algorithm seems to be successful at pinpointing high temperature events. Fig. 2 shows a temperature–space series and contour plot of the wavelet transform taken from case 1. The asterisks identify high temperature events that deviate from the mean by 0.05 °C. From the figure it is clear that the algorithm is able to perform a multi-scale filtration of the data to reveal high temperature events associated with cohesive groups at both large and small scales. The high temperature events identified by the asterisks at small and large wavenumbers are visibly correlated with large and small temperature fluctuations respectively in the temperature signal. Some asterisks do not lie directly at the points of maximum temperature in the signal. This is due to the inner product associated with the convolution which attempts to make the best fit of the Morlet wavelet to the data and occasionally falls short of locating temperature events in agreement with the actual peaks in the temperature signal.

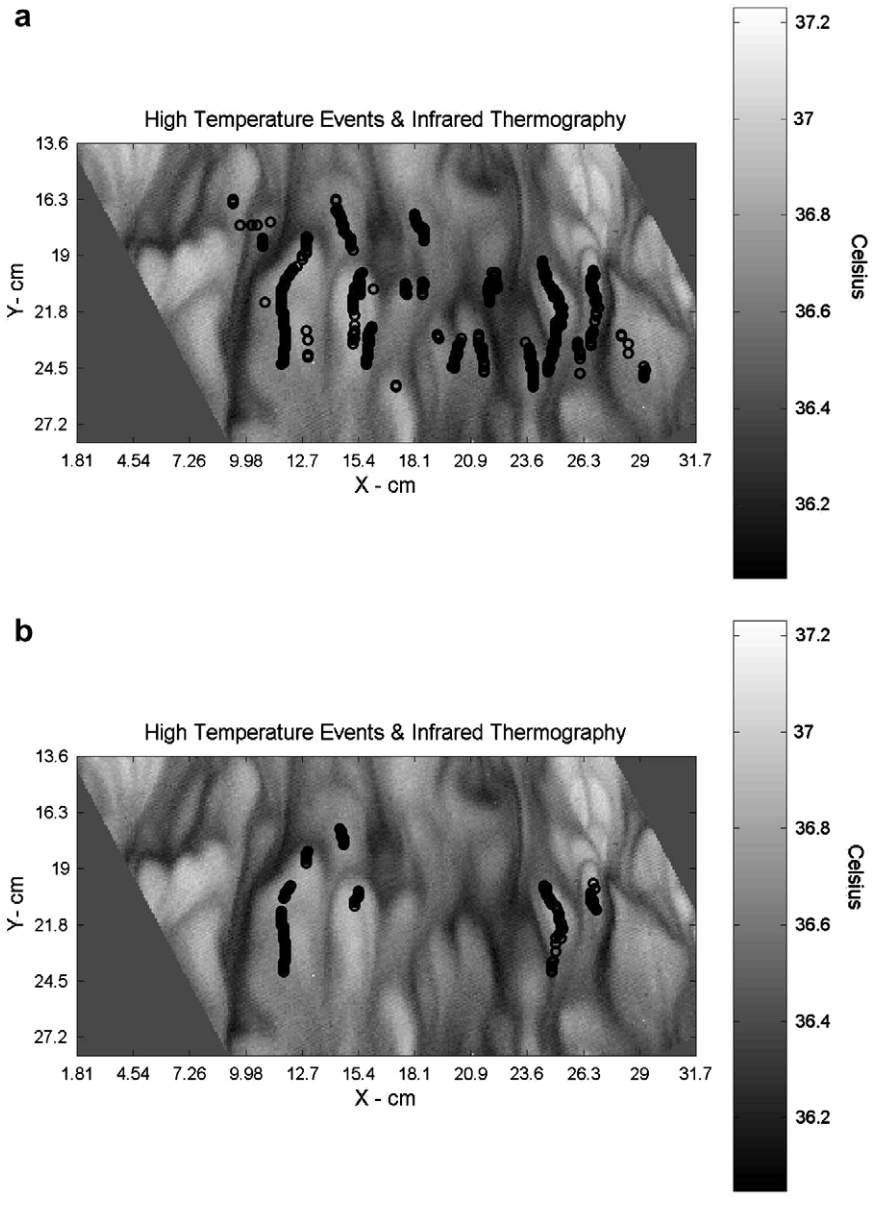

Fig. 3. (a) High temperature event information plotted as circles on top of the infrared imagery for 100 cross-wind scan lines. Wind speed is 2.9 m/s and temperature threshold is 0.1 °C and (b) High temperature event information plotted as circles on top of the infrared imagery for same image. Temperature threshold is 0.125 °C.

4.2. Spatial structure of high temperature events

Fig. 3a and b displays the spatial distribution of high temperature events found for 100 consecutive cross-wind scan lines from one image laid on top of the infrared imagery for case 1 at temperature fluctuation thresholds $T = 0.1$ °C and $T = 0.125$ °C. All high temperature events are indicated by circles. In Fig. 3a and b, the wind is blowing from top to bottom. It appears again that the wavelet analysis algorithm is successful at tracking the high temperature events at a specific temperature threshold as most of the circles lie on top of the cohesive thermal fish-scale structures.

4.3. Relationship of high temperature event statistic, $H_T(k)$ to friction velocity, u_w^* for cool-skin and warm-skin cases

Fig. 4a–d shows the high temperature statistic for cases 1–4. All wind speeds show, at low temperature fluctuation thresholds, a broad band of scales for the average number of high temperature events per unit area found in the cross-wind scans. This is readily seen in case 1 at the lowest temperature fluctuation threshold of 0.05 °C. Here, the high temperature statistic $H_T(k)$ slopes continuously to the right over the entire wavenumber range delineating that when considering both high and low temperature events in the surface temperature field, there are more high wavenumber (small scale) than low wavenumber (large scale) events. However, as the threshold is gradually increased, which excludes the low amplitude temperature fluctuations, a characteristic scale emerges in $H_T(k)$.

The distribution at high thresholds is qualitatively similar to the Rayleigh distribution of surface streaks found in the direct numerical simulations of Tsai et al. (2005). We note that as the temperature threshold is increased, $H_T(k)$ becomes increasingly characterized by statistical variability. This is because at such a high threshold, there are statistically fewer high temperature events. The charac-

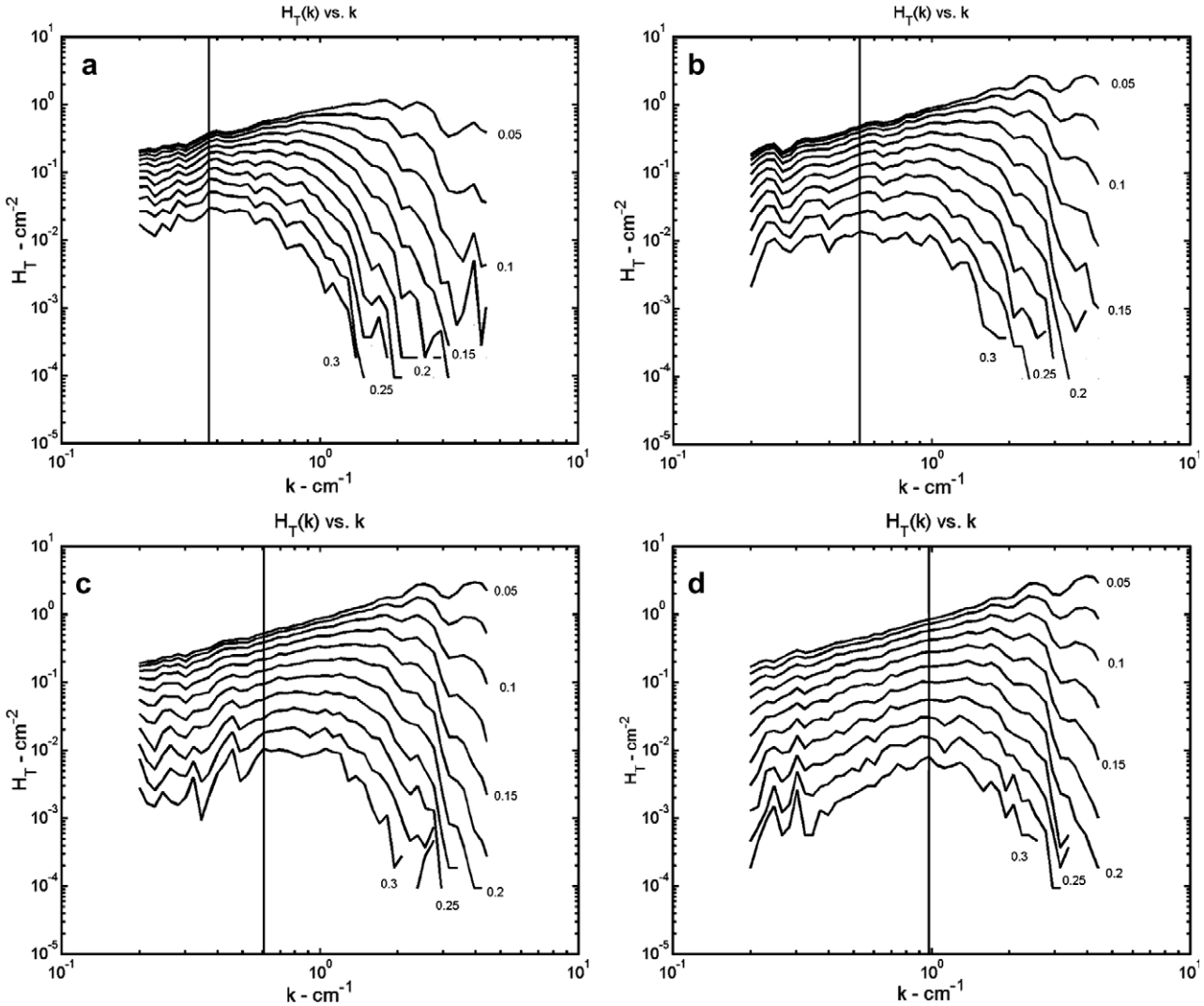

Fig. 4. High temperature statistic, $H_T(k)$ versus wavenumber, k for four different mean wind speeds from cool-skin regime: (a) 1.9 m s^{-1}, (b) 2.9 m s^{-1}, (c) 5.0 m s^{-1} and (d) 7.0 m s^{-1}. Temperature threshold in °C appear next to each curve and decrease in value vertically downward. Temperature threshold delineated for every other curve starting from the top curve.

teristic scale is obtained by finding the maximum value of the high temperature statistic at the highest temperature threshold before $H_T(k)$ becomes overwhelmed by statistical variability. This occurs at 0.3 °C and the characteristic scales for each case are delineated by the vertical line in the figures. This threshold is consistent with the maximum temperature variance of the data as reported by Smith et al. (2007) who found temperature fluctuations on the order of 1 °C which is nearly twice the temperature fluctuation threshold of 0.3 °C.

With an increase in wind speed from 1.9 to 4 m s^{-1} shown in Fig. 4a–d, the curve at the highest temperature threshold of 0.3 °C seemingly collapses onto a wavenumber which progressively gets larger in value. Though a strict functional dependence in $H_T(k)$ cannot be made in any of the cases, in general, Fig. 4a–d show that at low wind speeds and at high temperature threshold, $H_T(k)$ has high values at low wavenumbers. However, there are an increasing number of high wavenumber scales as the wind speed is increased at these same high temperature thresholds. This is consistent qualitatively with the work of Schimpf et al. (2004) who analyzed the temperature structures in infrared images using Laplacian pyramids. They found that small scales (high wavenumbers) contributed more to the variance in the temperature at high wind speeds but that large scale structures (low wavenumbers) contribute more at low wind speeds.

Fig. 5 shows $H_T(k)$ for the warm-skin case. The range of temperature thresholds is much smaller than in the cool-skin case due to the fact that the deviation from the mean temperature is much smaller (Smith et al., 2007). However, the structure of the high temperature statistic shown here is similar to the cool-skin case that has a comparable absolute value for the flux Richardson number as shown in Fig. 4a. In addition, the characteristic scale as obtained from our methodology from case 5 is close in value to that obtained from case 1. The small difference between the characteristic scales found in the warm-skin case, which is purely shear dominated, when compared to the cool-skin case, which has shear and buoyancy, suggests that the fish-scale structure size is robust and is dependent predominantly on wind shear stress. This is consistent with the observations of Smith et al. (2007).

The inverse of the wavenumber (λ) associated with the characteristic scale obtained via wavelet analysis is shown as a function of the friction velocity, u_w^*, in Fig. 6. This is defined here as the scale λ_{T^*}. Error bars giving the 95% confidence limits are also shown. The detailed uncertainty analysis may be found in Appendix A. Tsai et al. (2005) and Melville et al. (1998) conducted studies which yielded scale statistics as a function of wind speed. Extensive comparison of these results could not be made with our results since the conditions were too dissimilar. However, our results are consistent with the trends demonstrated by each of the authors. In particular, our statistical scale results for the surface streaks or fish-scales and those found by Tsai et al. (2005) are both smaller than those found by Melville et al. (1998) for comparable winds.

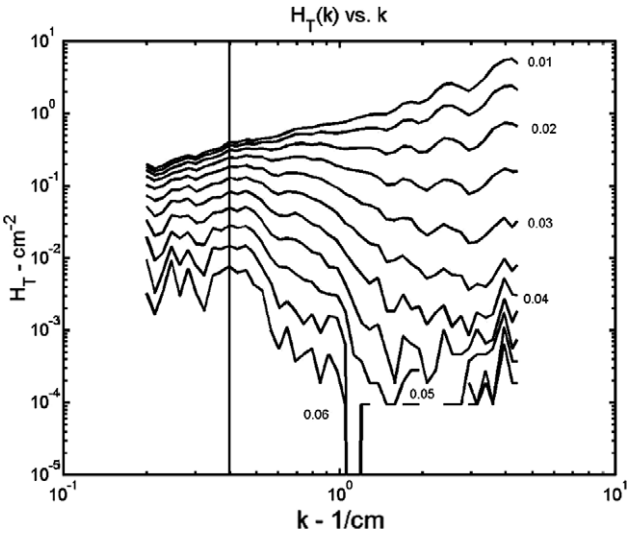

Fig. 5. High temperature statistic, $H_T(k)$ versus wavenumber, k from the warm-skin regime. Mean wind speed is 2.9 m s^{-1}. Temperature threshold in °C decreases vertically downward with values placed next to each curve. Temperature threshold delineated for every other curve starting from the top curve.

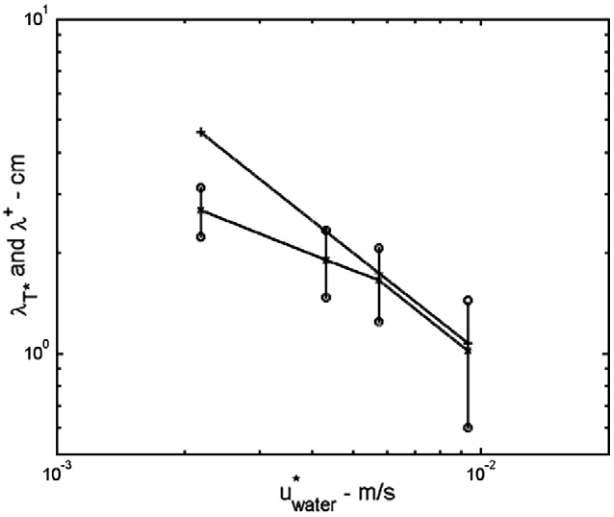

Fig. 6. Scale values obtained from wavelet analysis, λ_{T^*}, versus the water side friction velocity plotted as x's for cases 1–4. The theoretical curve from the equation, $\lambda^+ = \frac{100\nu}{u^*}$ also plotted as +'s. 95% confidence intervals for scales obtained from wavelet analysis are plotted as circles.

We note that at the wind speed of 5 m s^{-1} (case 4), surface waves appear at the interface. Extensive viewing of movies of the infrared images at this wind speed by Smith et al. (2007) show stable propagating quasi-linear thermal structures indicative of surface gravity waves. These structures do not appear in our results since the scale of the wave-induced thermal fluctuations is too large to be captured by this analysis. However, the slight change in the trend does seem to indicate a possible modulating effect by the surface waves. In addition, the large uncertainty indicated by the error bars in the observations for the highest friction velocity essentially shows that the value

of the thermal scale at this wind speed is not likely to be correlated with surface wind shear.

These estimated scales, $\lambda_T{}^*$, are physically akin to the streak spacing scales found in turbulent shear flows. This phenomenon was investigated by Nakagawa and Nezu (1981) and Smith and Metzler (1983) where coherent structures appeared spontaneously as instabilities when shear was exerted on the fluid surface. These structures were found to have a characteristic length scale in the direction transverse to the shear of approximately $\lambda^+ \sim 100\frac{\nu}{u_*^w}$. For comparison we also plot this scale in Fig. 6. The curve indicating this parameterization and the curve resulting from the wavelet analysis differ by less than an order of magnitude. However, the trends of both curves are similar in shape and suggest that the characteristic thermal cell size does scale inversely with friction velocity. The results also suggest that further analysis may allow for the possibility of using infrared remote sensing and the wavelet transform methods developed here to estimate wind shear at the air–water interface.

5. Conclusions

A wavelet based methodology is used to extract high temperature event statistics from IR imagery of a wind-driven air–water interface. At low wind speeds and within the air–water temperature differences used in the experiment, the algorithm detects high temperature events associated with coherent temperature groups in the cross-wind direction. The high temperature event statistics are shown to be broad-banded (in wavenumber space) at very low temperature thresholds. Increasing the temperature threshold brings forth a peak in the statistical distribution delineating a cross-wind characteristic scale. Analysis of the results shows that this scale gets smaller as the wind stress is increased, which is consistent with the classical streak spacing parameterization (Smith and Metzler (1983)) and with the results of Handler et al. (2001), Tsai et al. (2005) and Schimpf et al. (2004). The presence of steep and breaking waves makes the statistical scale results at large wind stress highly susceptible to error as delineated by the large error bars. The characteristic scale for the fish- scales for both the warm-skin and cool-skin cases, which possess similar absolute values for the flux based Richardson number, are also established as similar in magnitude. This suggests that the fish- scale structure is due to a shear instability, which is consistent with the previous observations of Smith et al. (2007). Because of the lack of understanding of whether wave-turbulent interactions or turbulent shear instabilities are the dominant processes in nature causing these fish-scale structures or streaks, it is not clear whether this methodology can definitively yield wind stress. Nevertheless this work suggests that at low wind speeds, in the absence of surface waves, the scale statistics of thermal instabilities do follow a trend which may, upon further intense analysis, yield estimates of wind stress when remote sensing infrared imagery is available.

Acknowledgements

This research was supported by the National Research Council Research Associateship Programs at the Naval Research Laboratory. Funding to conduct the experiments was provided to RSMAS by the Office of Naval Research under award N00014-03-1-0384. We also gratefully acknowledge assistance of Prof. Peter Minnett and other staff members at the Rosenstiel School (RSMAS) of the University of Miami.

Appendix A

The extent to which the results presented here depend on the particular choice of wavelet in the analysis methodology is a critical issue. The use of the Morlet wavelet is justified by the need for finding an 'atom' that possesses a structure that is local and quasi-periodic. In keeping with this idea, this analysis is based on the search for local periodic temperature fluctuations in the cross-wind direction of the data. The Morlet wavelet clearly has a structure that allows for the detection of local wave-like groups in temperature data.

A question that is pertinent to the evaluation of the developed methodology is the dependence of the results on the number of waves in the Morlet wavelet packet. Morlet wavelets of wavenumbers $K_0 = 5/2\pi,\ 6/2\pi,\ 7/2\pi, \ldots$ are all admissible and it is important to understand the robustness of the results to changes in the Morlet wavelet. A sensitivity analysis was performed on the data using Mother wavelets with different K_0 values. For further information on this type of analysis see Scott et al. (2005).

The uncertainty intervals were obtained by considering as a sample all scales at the highest temperature threshold of 0.3 °C. Considering these scales as individual realizations from the Student t-distribution, the error bars can be expressed as

$$\left[\left(\bar{\lambda}_{T*} - \frac{\tilde{s}_N \times t_{M-1,\alpha/2}}{\sqrt{M}}\right) \leqslant \lambda_{T*} \leqslant \left(\bar{\lambda}_{T*} + \frac{\tilde{s}_N \times t_{M-1,\alpha/2}}{\sqrt{M}}\right)\right]. \tag{9}$$

The mean characteristic scale over the set of observations is designated as $\bar{\lambda}_{T*}$, M is the number of scales in the sample, $\tilde{s}_N$ is the square root of the sample variance, and $\lambda_T{}^*$ defined above is the true characteristic scale. The value $t_{M-1,\alpha/2}$ is obtained from the Student t-distribution table and is the value such that

$$\text{Prob}\left[t_{M-1} > t_{M-1,\frac{\alpha}{2}}\right] = \frac{\alpha}{2}, \tag{10}$$

where $\alpha = 0.05$ is the area under the Student t-distribution curve.

References

Addison, P., 2002. Illustrated Wavelet Handbook. Institute of Physics Publishing, Bristol, UK, pp. 1–384.

Bock, E.J., Hara, T., Frew, N.M., McGillis, W.R., 1999. Relationship between air–sea gas transfer and short wind waves. Journal of Geophysical Research 104 (C11), 25821–25831.

Dickey, T.D., Hartman, B., Hammond, D., Hurat, E., 1984. A laboratory technique for investigating the relationship between gas transfer and fluid turbulence. In: Brutsaert, W., Jirka, G.H. (Eds.), Gas Transfer at Water Surfaces, pp. 93–100.

Garbe, C., Schimpf, U., Jahne, B., 2004. A surface renewal model to analyze infrared image sequences of the ocean surface for the study of air–sea heat and gas exchange. Journal of Geophysical Research 109 (C08S15). doi:10.1029/2003JC001802.

Goupillaud, P., Grossman, A., Morlet, J., 1984. Cycle-octave and related transforms in seismic analysis. Geoexploration 23, 85–102.

Grinsted, A., Moore, J.C., Jevrejeva, S., 2004. Application of the cross wavelet transform and wavelet coherence to geophysical time series. Nonlinear Processes in Geophysics 11, 561–566.

Handler, R.A., Smith, G.A., Leighton, R.I., 2001. The thermal structure of an air–water interface at low wind speeds. Tellus 53A, 233–244.

Jessup, A.T., Zappa, C.J., Loewen, M.R., Hesany, V., 1997. Infrared remote sensing of breaking waves. Nature 385, 52–55.

Komori, S., Nagaosa, R., Murakami, Y., 1993. Turbulence structure and mass transfer across a sheared air–water interface in wind driven turbulence. Journal of Fluid Mechanics 249, 161–183.

McKenna, S.P., McGillis, W.R., 2004. The role of free-surface turbulence and surfactants in air–water gas transfer. International Journal of Heat and Mass Transfer 47, 539–553.

Melville, W.K., Shear, R., Veron, F., 1998. Laboratory measurements of the generation and evolution of Langmuir circulations. Journal of Fluid Mechanics 364, 31–58.

Nakagawa, H., Nezu, I., 1981. Structure of space–time correlations of bursting phenomena in an open channel flow. Journal of Fluid Mechanics 104, 1–43.

Schimpf, U., Garbe, C., Jahne, B., 2004. Investigation of transport processes across the sea surface microlayer by infrared imagery. Journal of Geophysical Research 109 (C08S13). doi:10.1029/2003JC001803.

Scott, N.V., Hara, T., Walsh, E.J., Hwang, P.A., 2005. Observations of steep wave statistics in open ocean waters. Journal of Atmospheric and Oceanic Technology 22, 258–271.

Scott, N.V., 2005. Estimating steep wave statistics using a wave gauge array. Applied Ocean Research 27 (1), 23–38.

Smith, C.R., Metzler, S.P., 1983. The characteristics of low-speed streaks in the near-wall region of the turbulent boundary layer. Journal of Fluid Mechanics 129, 27–54.

Smith, G., Handler, R.A., Scott, N.V., 2007. Observations of the structure of the surface temperature field at an air–water interface for stable and unstable cases. In: Garbe, C.S., Handler, R.A., Jähne, B. (Eds.), Transport at the Air Sea Interface – Measurements, Models and Parameterizations. Springer-Verlag, pp. 205–222.

Tsai, W.T., Chen, S.M., Moeng, C.H., 2005. A numerical study on the evolution and structure of a stress-driven free-surface turbulent shear flow. Journal of Fluid Mechanics 545, 163–192.

Wanninkohf, R., McGillis, W.R., 1999. A cubic relationship between air–sea CO_2 exchange and wind speed. Geophysical Research Letters 26, 1889–1892.

Zappa, C.J., Asher, W.E., Jessup, A.T., 2004. Microbreaking and the enhancement of air–water transfer velocity. Journal of Geophysical Research 109 (C08S16). doi:10.1029/2003JC001897.